Thermal, electrical, and mechanical properties of hard nitrogen-alloyed Cr thin films deposited by magnetron sputtering

Camille Pallier [a], Philippe Djemia [b], Daniele Fournier [c], Laurent Belliard [c], Jun Lu [a], Fredrik Eriksson [a], Per Eklund [a], Grzegorz Greczynski [a], Arnaud le Febvrier [a],*

[a] *Thin Film Physics Division, Department of Physics, Chemistry, and Biology (IFM), Linköping University, Linköping SE-581 83, Sweden*
[b] *Université Sorbonne Paris Nord, Alliance Sorbonne Paris Cité, Laboratoire des Sciences des Procédés et des Matériaux, UPR 3407 CNRS, F-93430 Villetaneuse, France*
[c] *Sorbonne Université, Centre National de la Recherche Scientifique, Institut des NanoSciences de Paris, UMR 7588, Paris 75005, France*

ARTICLE INFO

ABSTRACT

Cr—N based materials, including stoichiometric CrN and Cr:N with a wide range of nitrogen contents, are commonly used as hard and corrosion-resistant coatings. Cr-rich films in this materials system can retain the bcc structure of metallic Cr with few percent of dissolved nitrogen, which can be used for tailoring the mechanical, thermal, and electrical properties. Here, we investigated low nitrogen containing Cr thin films deposited by high ion assisted magnetron sputtering with a substrate temperature of 200 °C. With the gas flow ratio maintained at $f_{N2/Ar} = 0.02$, the substrate bias and the target power allows for control of the film composition ($0.03 < N/Cr < 0.34$). The films comprise a mixture of bcc-Cr and hexagonal $Cr_2N_{1-\delta}$ phases. The mechanical properties studied by nanoindentation and Brillouin inelastic light scattering revealed a hardening effect due to the multiphase nanostructure. The mechanical properties of the Cr:N films depend on the residual stress, on the amount of h-$Cr_2N_{1-\delta}$ phase and on the nanostructuring nature of the coatings. A maximum hardness of 37 GPa was achieved for a dense film with a Young's modulus of 340 GPa, a shear modulus of 118 GPa, and a relatively low thermal conductivity of 7 W/mK.

1. Introduction

Controlling the combination of elastic, mechanical, electrical, and thermal properties in technologically relevant coating materials is of importance in application as hard coatings for cutting tools or corrosion-resistant conductive coatings for fuel cells, batteries, or electrolysis cells. Physical vapor deposition (PVD) techniques using magnetron sputtering is a commonly used techniques for the deposition of these types of coatings. Widely investigated, it has led to a vast knowledge on control of growth enabling desired properties and phase formation to be achieved. Transition metal nitride-based material systems are one the most studied materials system for such applications [1–3]. They are hard and tough with relatively low thermal conductivities, and low electrical resistivity being metals or narrow-bandgap semiconductors. The mechanical, thermal, and electrical properties of the transition nitride films are influenced by different orientations of grains, morphologies, residual stresses, and the variation of point defects induced during the growth [1,4–12].

Cr—N based materials are important model systems because of their use in hard coatings, thermal applications, diffusion barrier coatings and for thermoelectric properties [13–20]. In this materials system, different phases can coexist depending on the nitrogen content bcc-Cr/h-Cr_2N or Cr_2N/CrN [6,7]. The fully Chromium nitride, CrN, in its rock-salt structure, has been seen as a possible replacement for TiN with its remarkable mechanical properties with a hardness and reduced Young's modulus ranging around 20–28 GPa and 300–350 GPa, respectively [4,6,7,21,22].

In contrast, for Cr:N films with low N content, nitrogen can be introduced in the bcc lattice as dopants or alloying elements (interstitial solid solution with few percent ≤4%) and may increase hardness and Young's modulus. Previous studies of Cr:N (≤ 5 at. % N) films showed that by tailoring the microstructure the desired properties could be achieved [6,7,23]. A comparison of Cr:N films with 5–33 at.% N showed that, in contrast to DC-sputter-deposited films with columnar growth, HiPIMS, with its high degree of ionized sputtered metal flux, allowed for a fine-grained nanocrystalline structure, leading to higher hardness of

---

28 GPa of the material [21,24].

Physical vapor deposited Cr:N thin films may therefore become a replacement for electroplated hard chrome. An alternative to HiPIMS is to use ion-assisted growth where a solenoid coil provides a high ion flux to the growing film. This technique allows to influence the density of Ar ions near the substrate and therefore enhance the effect of substrate biasing [25]. Moreover in the material system studied, these layers have the advantage of combining a unique combination of physical properties with their high electrical properties, high hardness and ductility [24]. Similar studies on single metals or binary nitrides have shown prospects for controlling the film growth, thus the final properties of the material [26–29]. There are still unexplored aspects in the Cr:N materials system such as the study of the Cr-rich side of Cr:N material system using Ar ion assisting magnetron sputtering where morphology and crystallographic orientation can be tailored to another extend.

In the present paper, we investigated the microstructure, mechanical, electrical, and thermal properties of DC sputter-deposited Cr:N films with magnetic field assisted-magnetron sputtering. Two different series of samples were studied in which the amount of nitrogen incorporated in the films was controlled between 2 and 25%. The results show the possibility to deposit non-columnar, nanostructured films with smooth surface using a low temperature DC magnetron sputtering processing. The different characteristics (phase, morphology) of the films were analysed to understand resulting mechanical, thermal, and electrical properties of the films. We demonstrated the possibility to obtain bcc-Cr and h-Cr_2N dense nanocomposite films in which the nanostructuring and multiphase formation led to an overall improvement of the mechanical, thermal, and electrical properties.

2. Experimental details

Cr:N films were deposited by reactive magnetron sputtering a high vacuum chamber (base pressure of ~3 × 10^{-7} Pa). The deposition temperature was fixed at 200 °C since this yield (nano)crystalline films (see, e.g., [24]), while still being sufficiently low to allow deposition onto a wide range of temperature-sensitive metallic substrates. The depositions were made in a flow-controlled Ar (99.999% pure)/N_2 (99.999% pure) gas mixture with a total flow of 45 sccm, corresponding to a total pressure of 0.53 Pa (4 mTorr). The gas flow ratio was maintained at $f_{N2/Ar}$ = 0.02. The chromium source was a 75 mm-Cr target (99.95% of purity). More details on the deposition chamber can be found elsewhere [30]. For the two series of experiments, a solenoid coil, serving to increase the plasma density near the substrate position, was used with an applied current of 5 A, an optimized coil condition for similar material systems [30]. The Al_2O_3 (c-cut) substrates (10 × 10 mm^2) (Alineason Materials and Technology) were cleaned in Hellmanex (3 min), water (5 min), acetone (10 min) and ethanol (10 min) in an ultrasonic bath and finally blown dry by N_2 gas (the cleaning procedure is detailed elsewhere) [31]. Prior to each deposition, the temperature was maintained at 200 °C for 1 h. The floating potential at the substrate position was measured to be about -12 V. For the substrate-bias series, the Cr-target power was maintained at 75 W when the substrate bias was set between −30 V, −75 V and − 100 V (values above the floating

potential). For the target-power series, the substrate bias was fixed at −75 V and Cr-target power was set to 50 W, 75 W, 100 W. Each experiment time was 30 min, resulting in film thicknesses in the range from 160 to 310 nm. The different samples with their respective series and different conditions are listed in Table 1.

X-ray photoelectron spectroscopy (XPS) spectra were recorded in a Axis Ultra DLD instrument from Kratos Analytical (UK). The base pressure during spectra acquisition was better than 1.1 × 10^{-9} Torr (1.5 × 10^{-7} Pa). Monochromatic Al K_a radiation (h_γ = 1486.6 eV) with the X-ray anode operated at 150 W was used. All core-level spectra were referenced to the Fermi level cutoff, which defines zero binding energy (BE) [32]. Spectra were acquired with a pass energy of 20 eV, which results in a full width at half maximum (FWHM) intensity of the calibration-sample Ag $3d_{5/2}$ core-level peak of 0.47 eV. Before XPS analyses, samples were sputter-etched with 4 keV Ar^+ ions incident at 70° with respect to the surface normal for 2 min. The ion energy was then reduced to 0.5 keV for 10 min to minimize sputter damage [33]. The Ar^+ ion beam was rastered over an area of 3 × 3 mm^2 and XPS spectra were obtained from the center (0.3 × 0.7 mm^2) of the etched region.

X-ray diffraction (XRD) was performed on performed on an X'Pert PRO MRD diffractometer from PANalytical using Cu $K_{\alpha1-2}$ radiation with a nickel filter in Bragg-Brentano configuration (θ-2θ scans) and on a four-circle diffractometer Philips X'Pert-MRD with monochromatic Cu $K_{\alpha1}$ radiation equipped with a hybrid mirror and a triple axis optics for X-ray reflectivity (XRR). Fitting of the XRR measurements was performed with the X'Pert Reflectivity software (PANalytical) where the average density of the film was extracted. A theoretical density ($\rho_{theor.}$) was approximated and calculated from the composition of the film as measured by XPS considering a mix of a bcc-Cr and a h-$Cr_2N_{1-\delta}$ phases using the following formula:

$$\rho_{theor.} = \frac{x \times \rho_{Cr2N} + (1 - 2x) \times \rho_{Cr}}{x + (1 - 2x)} \qquad (1)$$

where x corresponds to the amount of $Cr_2N_{1.85}$ phase in the film, ρ_{Cr2N} and ρ_{Cr} are the bulk densities of Cr_2N (without nitrogen vacancies) and Cr, respectively, from the International Centre for Diffraction Data (ICDD) data file (Bulk Cr_2N: 6.73 g/cm^3, bcc-Cr: 7.19 g/cm^3). Finally, the apparent density is estimated according to:

$$\text{Apparent density} = \frac{\rho_{XRR}}{\rho_{theor.}} \qquad (2)$$

Here, ρ_{XRR} is the density estimated by XRR, and $\rho_{theor.}$ is the density calculated from the Eq. (1).

Scanning electron microscopy (SEM) was carried out with a LEO 1550 Gemini SEM at an accelerating voltage of 10 kV. Transmission electron microscopy (TEM) analysis was carried out on FEI Tecnai G2 TF20 UT microscope operated at 200. Cross-sectional samples were prepared by placing the cut samples in a titanium grid, following by manual polishing on diamond papers until the thickness reaches about 60 μm. The sample was then thinned using a Gatan Precision Ion Polishing System (PIPS) (Ar^+ ion milling), first at 8° and 5 keV for 2 h, following by milling at 5° and 5 keV for an average of 4 h – until reaching electron transparency – and then a final polishing step at 5° and

Table 1

Composition of the Cr:N films (estimated by XPS) for the two series of samples (target-power and substrate-bias) and the thickness determined by cross-sectional SEM images.

	Series Parameter (target power/substrate bias)	Common Parameter (substrate bias / target power)	at. % Cr	at. % N	at. % O	Thickness (nm)	Sample name
Target-power series	100 W	−75 V	95	3	2	310	$Cr_{0.97}N_{0.03}$
	75 W	−75 V	84	14	2	260	$Cr_{0.86}N_{0.14}$
	50 W	−75 V	73	25	2	160	$Cr_{0.75}N_{0.25}$
Substrate-bias series	−100 V	75 W	96	2	2	260	$Cr_{0.98}N_{0.02}$
	−75 V	75 W	84	14	2	260	$Cr_{0.86}N_{0.14}$
	−30 V	75 W	76	18	6	250	$Cr_{0.81}N_{0.19}$

0.8 keV for 2 h. Samples were examined in bright field mode and their selected area electron diffraction (SAED) patterns were recorded.

The electrical resistivities of all samples were determined by measuring the sheet resistances of the films measured by a four-point-probe Jandel RM3000 station. The resistivity was obtained by multiplying the sheet resistance with the sample thickness, which was obtained from cross-section SEM images and corrected, if necessary, with the off tilting.

The mechanical properties (hardness and reduced elastic modulus) of the Cr:N films were investigated by nanoindentation using a Triboindenter TI 950 (Hysitron) and a Berkovich diamond tip with an apex radius of 100 nm. The mechanical response of the thin films was recorded for 30 nano-indents per sample at a constrained load of 500 μN, corresponding to a minimum penetration depth of 12 nm (<10% of the thinnest sample). The data were analysed using the approach of Oliver and Pharr [34].

Time-resolved measurements of longitudinal sound velocity V_L were performed using a standard picosecond laser ultrasonics (PLU) setup [35,36]. The pump and probe beams, emitted simultaneously by a mode-locked Ti:Sapphire Tsunami Spectra-Physics laser source operating at 800 nm with a repetition rate around 79.3 MHz, are focused by means of a long working distance lens on the film. Following the modulated pump absorption, an ultrafast lattice deformation is induced, creating a coherent acoustic pulse at the free surface. This longitudinal acoustic wave propagating in the system along the z axis is partly transmitted and reflected at the film/substrate interface and finally detected through the transient sample reflectivity change at the free surface using the time delayed probe beam. Knowing the sample thickness (t), the mass density (ρ) and measuring the time of flight (TOF) in the film, the longitudinal sound velocity $V_L = 2\,t/TOF$ of the film could be obtained, and the longitudinal elastic constant/modulus along the growth axis $C_{33} = \rho(V_L)^2$ calculated.

Brillouin inelastic light scattering (BLS) was analysed by means of a Sandercock-type 3 + 3 pass tandem Fabry-Perot interferometer, in the back-scattering geometry, considering the coupling of the incoming light having wave vector k_i and frequency f_i, with the surface acoustic waves of wave vector Q and frequency f (see Refs. [11,37] for details). The inelastic scattered light having wave vector k_S and frequency f_S satisfies the following Conditions (3), (4) and (5):

$$k_s = -k_i \tag{3}$$

$$(k_s - k_i)_\| = \pm Q \tag{4}$$

and

$$f_s - f_i = f \tag{5}$$

The surface acoustic waves (SAW) are propagating along one in-plane direction with a wave vector modulus Q) defined as:

$$Q = \frac{4\pi}{\lambda_L}\,sin(\theta) \tag{6}$$

where λ_L the wavelength of the incident laser beam (532 nm) and θ the angle of incidence of the light with respect to the perpendicular z-axis. For an opaque film, the main feature appearing in a BLS spectrum is the Rayleigh surface wave peak having the lowest frequency f_R and sound wave velocities (V_R) defined by

$$V_R = 2\pi\,\frac{f_R}{Q} \tag{7}$$

All spectra obtained for different Q were fitted by considering the dynamical corrugation u_z^2 (f, z = 0) induced by the vertical atomic displacement u_z at the free surface, as being the only active ripple mechanism responsible of the inelastic light scattering [38,39]. Isotropic elastic properties approximation with two independent elastic constants C_{44} (shear modulus) and C_{33} was considered.

Thermal conductivity of the films was obtained using modulated thermoreflectance microscopy (MTRM). In this setup, a pump beam at 532 nm delivered by a Cobolt MLD laser, intensity modulated by an acoustic-optical modulator at a frequency f, is focused on the surface of the sample with an objective lens (N.A. = 0.5). The samples were coated by a 100 nm gold layer, ensuring that the heat source is located at the surface. Then, thermal waves are excited in the sample and monitored by the reflectivity surface change recorded around the pump location by another focused laser beam. We use a 488 nm Oxius laser to maximize the probe sensitivity to the thermal field in the gold cap layer. A photodiode and a lock-in amplifier record the AC reflectivity component, in a frequency range between 1 kHz and 1 MHz. Finally, the amplitude and phase experimental profiles were fitted according to a standard Fourier diffusion law to extract the thermal conductivity of the films [40,41]. Detailed procedure from experimental to data treatment can be found elsewhere [42].

3. Results

Table 1 presents the chemical composition of the Cr:N films analysed by XPS, and the thickness of the films measured from the cross-sectional SEM images. All the films have ~2 at. % of oxygen contamination, with one exception for the sample deposited using a low bias with 6 at.%. The nitrogen content in the film varies between 2% and 25%, thus in the Cr-rich side of the Cr—N system with the overall composition between Cr and Cr_2N. In the target-power series, an increase of the Cr-target power from 50 to 100 W led to a variation of nitrogen content in the film from 3% to 25%. In the case of the substrate-bias series, the nitrogen content in the films decreases from 18% to 2% for an increase of the substrate bias from −30 V to −100 V. For the rest of the article, we will consider two series of samples, denoted as $Cr_{1-x}N_x$ with x corresponding to the percentage of nitrogen, and arranged by the composition of the film.

Fig. 1 shows the Cr2p and N1s XPS core-level spectra from the two series of sample. Even with a difference in composition in the nitrogen content in the film, no clear differences are observable on the Cr 2p spectra within a series of sample (Fig. 1a). No shifting of the peak position (Cr $2p_{3/2}$ at 274.4 eV) is observed but an asymmetry of the peak is getting pronounced on the higher binding energy side of the Cr 2p peaks when the nitrogen content in the film increases. This observation reveals that the peak could be composed of two components: a metal Cr component (from NIST X-ray Photoelectron Spectroscopy Database: metallic Cr $2p_{3/2}$ reported at 574.3 eV [43]) still present even for the highest nitrogen content film (25%) and a nitride component at higher binding energy. On the N 1 s peak, no shifting of the peak position is observed but two components could be distinguished. The main peak is situated at 398.0 eV and a shoulder peak at lower BE. This feature has already been observed on similar studies where the Cr:N films were grown using HiPIMS [24]. It has been observed that the N1s spectra shape does not differ between a pure bcc-Cr with dissolved nitrogen or a pure Cr_2N with the two components peaks on N1s. As reference from the NIST XPS database, the Cr_2N phase (the intermediate phase in the Cr:N material system) has been reported with the Cr $2p_{3/2}$ at 574.8 eV and N 1 s at 397.4 eV and the CrN $2p_{3/2}$ at 575.7 eV [43].

Fig. 2a shows θ-2θ X-ray diffractograms of Cr:N films for a target-power series varying form 50 W to 100 W leading to films with compositions varying between $Cr_{0.75}N_{0.25}$ to $Cr_{0.97}N_{0.03}$. Except for the sharp substrate peak at 2θ = 41.6°, the diffraction peaks from the films are broad where several overlapping peaks can be present between 38° and 46°. The broad peak situated at 2θ = 44° is identified as the 110 reflection from bcc—Cr. This peak is located at the same position for all samples within the target-power series. Note here, that compared to the unstressed bcc-Cr reference, the diffraction peaks appear to be shifted to lower angle. The peaks (0002 and 11$\bar{2}$1), identified as an isotype structure as h-Cr_2N phase situated at a 2θ angle lower than 41.5°, became more defined and shift to lower diffraction angles when the
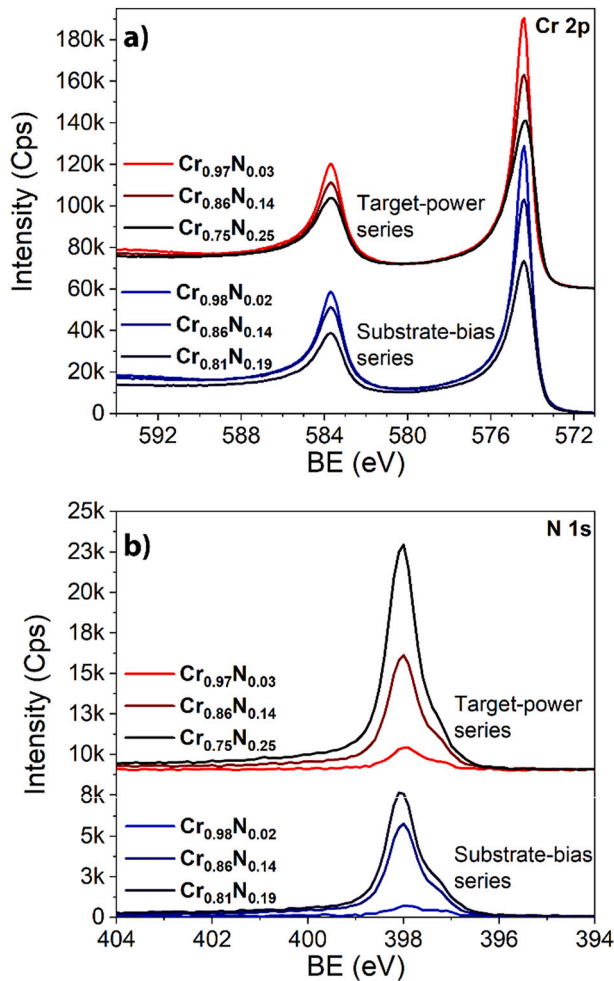
Fig. 1. a) Cr 2p and (b) N 1 s XPS core-level spectra obtained from the samples in the two series (target power and substrate bias series).

Fig. 2. a) XRD θ-2θ measurements of Cr:N thin films in the target-power series with film composition between $Cr_{0.75}N_{0.25}$ to $Cr_{0.97}N_{0.03}$; b) Relative 2θ position compared to their respective ICDD data peak position for the bcc-Cr 110 reflection peak and the h-Cr_2N 0002 and $11\bar{2}1$ reflection peaks. The ICDD data reference material corresponds to the bulk stress-free material of bcc-Cr (01–076-2494) and h-Cr_2N (00–035-0803). Peak maked as * correspond to the substrate (0006 of c-plane Al_2O_3).

nitrogen content increases. Moreover, as the $11\bar{2}1$ reflection of h-Cr_2N phase is the most intense peak in a randomly oriented films (ICDD 00-035-0803), the relative intensities of 0002 and $11\bar{2}1$ peaks reveal some degree of 0002 preferential orientation of the films especially for the highest nitrogen containing film.

Fig. 2b presents the relative evolution of the XRD peak position for the two phases in comparison with their ICDD reference data in their stress-free bulk polycrystalline forms. The relatively constant value of diffraction angle for the bcc-Cr phase reveals a similar stress level within the series when applying the same substrate bias of −75 V. In contrast, the peak positions of the h-Cr_2N shifts towards lower angle for the highest nitrogen content film. The h-Cr_2N can accommodate a wide variation of nitrogen composition while retaining the hcp structure: Cr_2N to $Cr_2N_{0.76}$ [44]. This explains that at high nitrogen content, the film is most probably composed of a mixture of bcc-Cr phase and a quasi-stoichiometric h-Cr_2N_1 phase while at low nitrogen content, it most likely that the film is composed of a mixture of bcc-Cr phase and a sub-stochiometric h-$Cr_2N_{1-\delta}$ with a high amount of nitrogen vacancies.

Fig. 3a shows θ-2θ X-ray diffractograms of Cr:N films in the substrate-bias series. In Fig. 3b, the XRD peaks positions relative to corresponding ICDD reference values for stress-free bulk samples is displayed. Similarly to the target-power series, the films are composed of a mixture of a bcc-Cr and aCr2N-isotype phase ($Cr_2N_{1-\delta}$) in which the ratio between the two phases proportions varies with the nitrogen content. At the difference of the target-power series, the position of the bcc-Cr 110 peak shift towards lower angles when the substrate bias increased. The peaks identified as
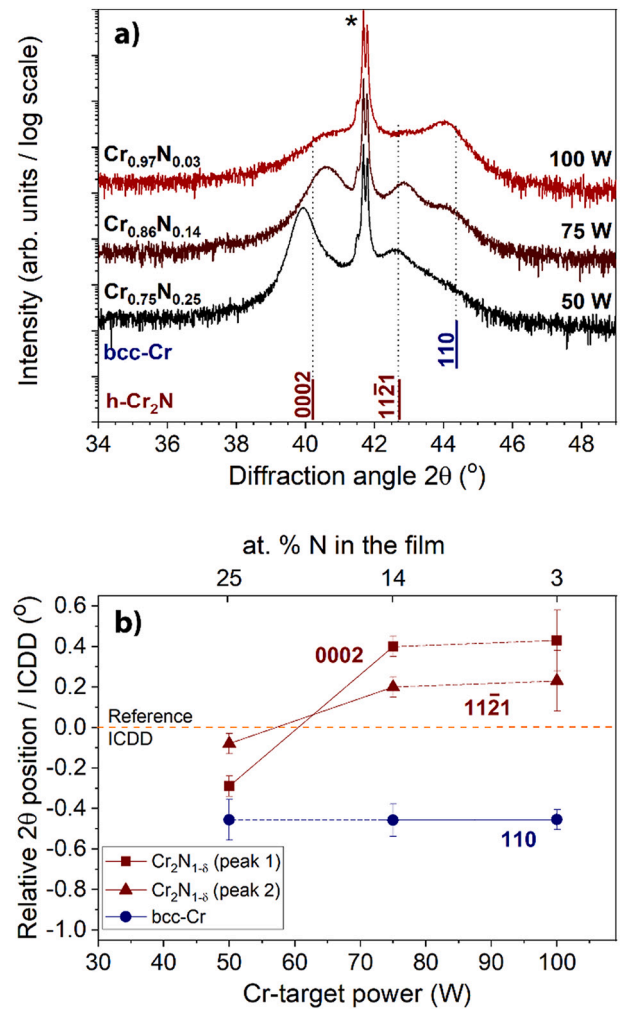
h-$Cr_2N_{1-\delta}$ shifted to the same extend to lower angles.

Fig. 4 presents the bright field TEM images and the SAED pattern obtained from films grown in the target-power series with the composition $Cr_{0.97}N_{0.03}$ and $Cr_{0.86}N_{0.14}$. For both samples, the bright field TEM images show variation of contrast and Moiré fringes characteristics of different orientation of crystallographic domains. As it can be seen from the Fig. 4b, at the interface region, the film $Cr_{0.97}N_{0.03}$ consists of equiaxed nanograin with average diameter of approximately 5 nm. Above the layer, column-like grains grew, with columnar diameter of 10 nm and 20 nm in length. The film $Cr_{0.97}N_{0.03}$ has similar microstructure features with crystallite size in the same range (10–20 nm). For both films, the SAED pattern (Fig. 4c-d) confirms the existence of poly-crystalline bcc-Cr and h-$Cr_2N_{1-\delta}$ phases observed by the presence of multiple reflections and rings of diffraction: 200, 220, 310 (bcc—Cr) and $11\bar{2}2$, $30\bar{3}2$, 0002 (h-$Cr_2N_{1-\delta}$). Diffraction rings are observed for the film $Cr_{0.97}N_{0.03}$, while for the film $Cr_{0.86}N_{0.14}$, numerous spots of diffraction situated at the same d values forming a ring are observed. This difference between the two samples reveals some degree of texture in the film $Cr_{0.86}N_{0.14}$, which remains at a low level for a texture along the [0002] direction.

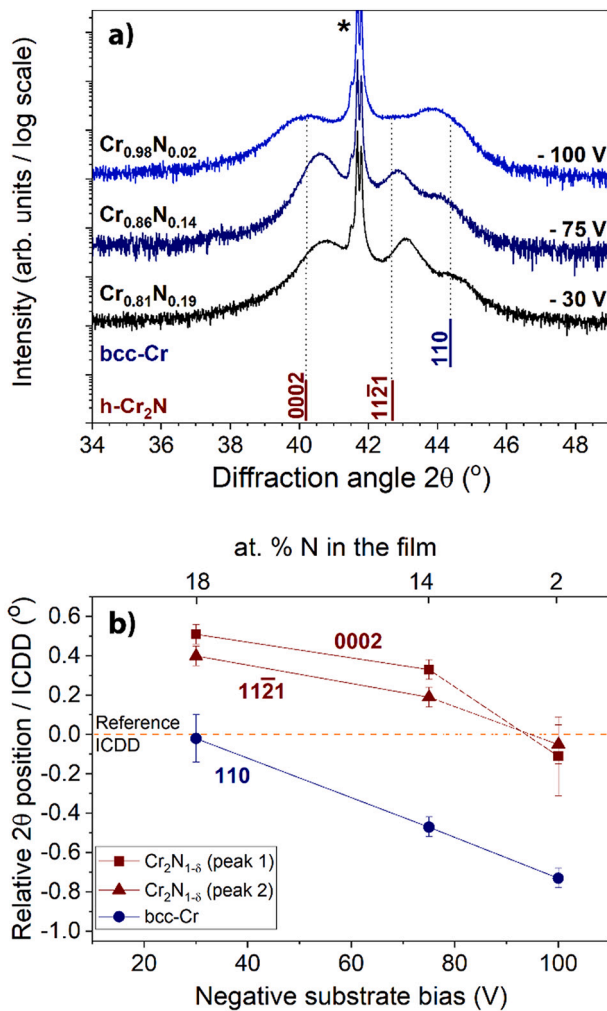Table 2 summarizes the sample details obtained from the XRD θ-2θ

Fig. 3. a) XRD θ-2θ measurements of Cr:N thin films in the substrate-bias series with film composition between $Cr_{0.81}N_{0.19}$ to $Cr_{0.98}N_{0.02}$; b) Relative 2θ position compared to their respective ICDD data peak position for the bcc-Cr 110 reflection peak and the h-Cr_2N 0002 and $11\bar{2}1$ reflection peaks. The ICDD data reference material corresponds to the bulk stress-free material of bcc-Cr (01-076-2494) and h-Cr_2N (00-035-0803). Peak maked as * correspond to the substrate (0006 of c-plane Al_2O_3).

XRD interpretation. The calculation leads to possible estimation errors because the nitrogen content in h-$Cr_2N_{1-\delta}$ is unknown and could be between $Cr_2N_{0.76}$ and Cr_2N. Nevertheless, this method gives a rough estimation of the proportion of the two phases present. By choosing to fix the vacancies at the maximum reported in literature ($\delta = 0.24$) [44], an over-estimation of Cr_2N % is probable for the highest nitrogen containing film where δ could be lower than 0.24 as seen by the error bar in Table 2.

In the target-power series, the film with the lowest amount of nitrogen has a mass density of 7.05 g/cm^3, close to the values of pure chromium (7.19 g/cm^3, ICDD 00–006-0694). The X-ray density in the target-power series decreases to 6.50 g/cm^3 when the amount of h-$Cr_2N_{1-\delta}$ phase increases. In the substrate-bias series, the X-rays density remains between 6.44 and 6.62 g/cm^3. Overall, the densities of the films are relatively close or lower than the Cr (7.19 g/cm^3). The calculated apparent density of the film differs between samples. Most of the films have an apparent density at 93–95% with two exceptions on the lowest nitrogen containing films. The film $Cr_{0.97}N_{0.03}$, in the target-power series, presents the highest apparent density with 98% (100 W Cr-target power, −75 V substrate bias). In contrast, the film $Cr_{0.98}N_{0.02}$, in the other series (75 W Cr-target power and −100 V substrate bias), with similar composition has an apparent density of 90%. An increase of the bias from −30 V to −100 V (sample $Cr_{0.81}N_{0.19}$ to sample $Cr_{0.98}N_{0.02}$) generated a diminution of the apparent density from 95% to 90%.

Fig. 5 presents the SEM top surface morphology and the Cross-sectional images of the Cr:N films in the two series. In the substrate-bias series, the film deposited with a higher substrate bias present a clear columnar growth with apparent porosity between the columns and clear grain edges on the top surface. A columnar growth is also observed when the substrate bias is reduced to −30 V (corresponding to lower amount of nitrogen), with a smoother surface morphology than the films deposited with −100 V. At a substrate bias of −75 V, the columnar growth is diminished with what will be describe as small grain aggregation along the film growth direction, and the grains are not clearly distinguished on the top-surface morphology giving a smooth surface. In the target-power series, generally the films appear dense and smooth. The SEM observations are in accordance with the estimation of the apparent density where for the film with the lowest amount of nitrogen, in the substrate-bias series, presents a lower apparent density.

Fig. 6 shows the mechanical properties determined from the nano-indentation, and from PLU and BLS analysis versus the h-$Cr_2N_{1-\delta}$ in the film (values reported in Table 3). In the target-power series, the hardness increases from 30 to 36 GPa when the h-$Cr_2N_{1-\delta}$ content increases while the reduced Young's modulus varies between 300 and 350 GPa. In the substrate-bias series, the trends are not as obvious. The hardness of the film varies between 23 and 34 GPa with a reduced Young's modulus varying between 290 and 350.
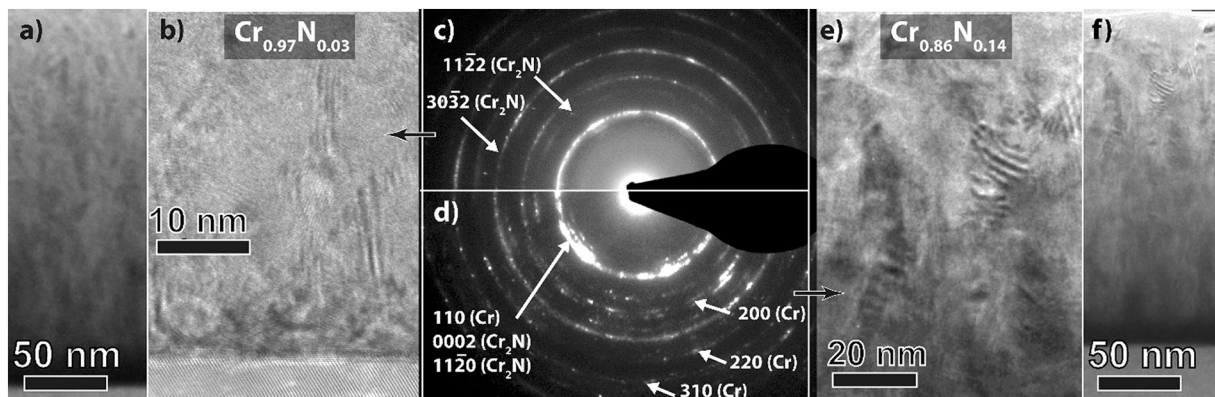
and the x-ray reflectivity analyses. The proportion of phases in the films can be estimated from the composition of the films and considering a mix of only a bcc-Cr and h-$Cr_2N_{1-\delta}$ ($\delta = 0.24$) and are consistent with the

Fig. 4. TEM analysis from of the films grown in the target-power series with the two different contents in nitrogen: $Cr_{0.97}N_{0.03}$ (a, b, c) and $Cr_{0.86}N_{0.14}$ (d, e, f). Cross-sectional Bright field images (a, b, e, f) and SAED pattern (c, d).

Table 2
Details of the XRD analysis, the density from XRR, the estimation of the apparent density of the materials. The proportion of the phases are calculated from the composition considering a mixture the bcc-Cr phase and either $Cr_2N_{0.88}$ or $Cr_2N_{0.76}$ for the $h-Cr_2N_{1-\delta}$ phase depending on the XRD results (the dominant phase is marked in bold).

	Sample	Phases	Proportion of phase in at. %		Qualitative residual stress	ρ_{XRR} (g/cm³)	ρ_{theor} (g/cm³)	Apparent density (±0.5%)
Target-power series	$Cr_{0.97}N_{0.03}$	**bcc-Cr**	**92**	(+**2%**)	Medium	7.05	7.15	98%
		$h-Cr_2N_{1-\delta}$	8	(−2%)				
	$Cr_{0.86}N_{0.14}$	**bcc-Cr**	**63**	(+**9%**)	Medium	6.55	7.02	93%
		$h-Cr_2N_{1-\delta}$	37	(− 9%)				
	$Cr_{0.75}N_{0.25}$	**bcc-Cr**	**34**	(+**15%**)	Medium	6.50	6.89	95%
		$h-Cr_2N_{1-\delta}$	57	(−15%)				
Substrate-bias series	$Cr_{0.98}N_{0.02}$	**bcc-Cr**	**94**	(+**1%**)	High	6.44	7.16	90%
		$h-Cr_2N_{1-\delta}$	6	(−1%)				
	$Cr_{0.86}N_{0.14}$	**bcc-Cr**	**63**	(+**9%**)	Medium	6.55	7.02	93%
		$h-Cr_2N_{1-\delta}$	37	(−4%)				
	$Cr_{0.81}N_{0.19}$	**bcc Cr**	**50**	(+**11%**)	Low	6.62	6.96	95%
		$h-Cr_2N_{1-\delta}$	50	(−11%)				

bcc—Cr: phase isotype as bcc-Cr with diluted nitrogen/oxygen.
$h-Cr_2N_{1-\delta}$: phase isotype as Cr_2N with nitrogen vacancies.
The proportion of phases are defined considering a nitrogen deficient $h-Cr_2N_{1-\delta}$ with $\delta = 0.24$ the error in % are from the possible uncertainty on $0 < \delta < 0.24$.
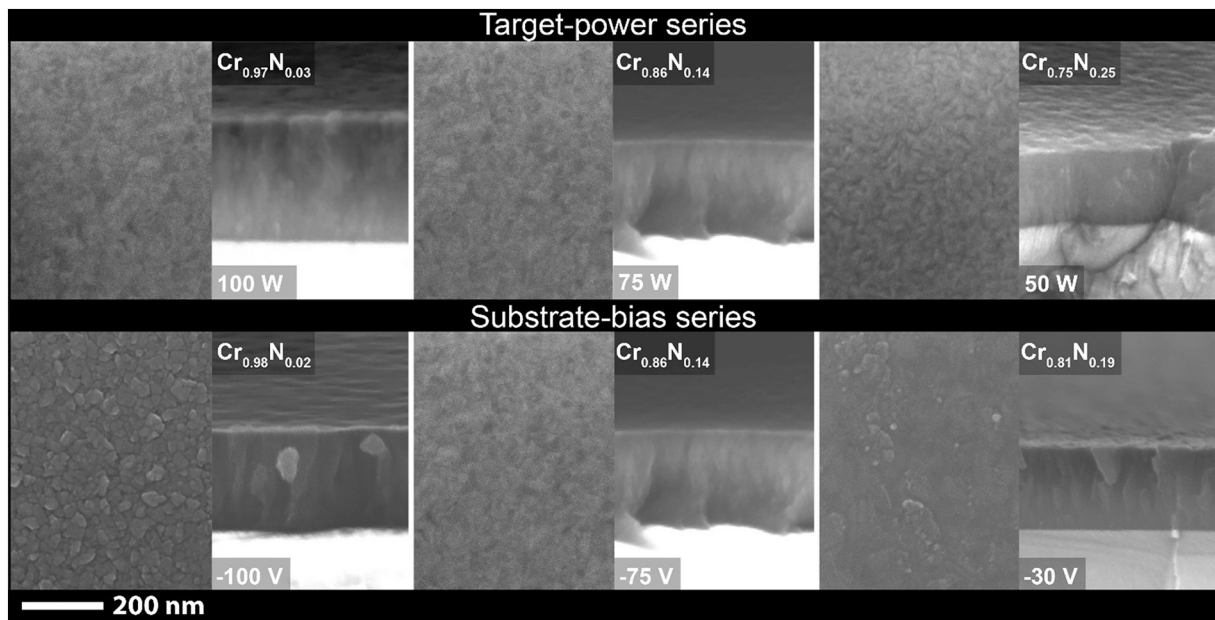

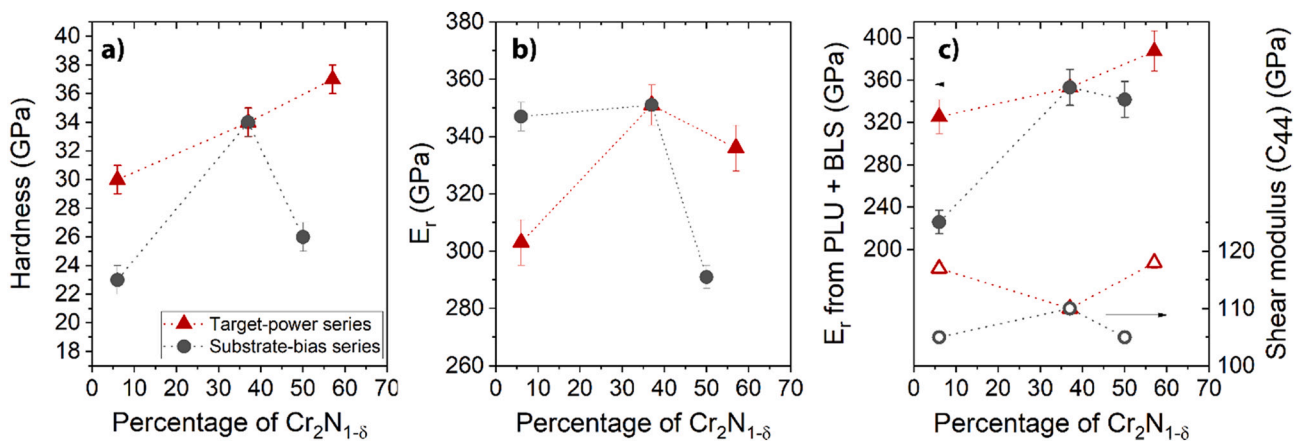**Fig. 5.** SEM top surface and cross-sectional images of: Cr:N thin films: in both series (target-power substrate-bias).

Fig. 6. Mechanical properties of the two series (target-power and substrate-bias) versus the content of $h-Cr_2N_{1-\delta}$ in the film: a) hardness measured by nano-indentation; b) Reduced Young's modulus (E_r) measured by nanoindentation. c) Reduced Young's modulus and shear modulus $G = C_{44}$ estimated by Brillouin inelastic light scattering (BLS) and picosecond laser ultrasonics PLU) techniques.

Table 3

summary of the mechanical properties, thermal and electrical conductivity of the films.

Series	Sample	nanoindentation		PLU + BLS					Thermoreflectance		Resistivity
		E_r (GPa)	H (GPa)	E (GPa)	E_r (GPa)	C_{33} (GPa)	C_{44} (GPa)	υ	κ (W/mK)	D ($\times 10^{-7}$) (m²/s)	$1/\sigma$ (± 5 μΩcm)
Target-power series	$Cr_{0.97}N_{0.03}$	303	30	299	325	384	117	0.281	7	10	65
		± 5	± 1	± 15	± 16	± 19	± 1				
	$Cr_{0.86}N_{0.14}$	351	34	302	353	557	110	0.377	8	7	170
		± 7	± 1	± 15	± 17	± 22	± 1				
	$Cr_{0.75}N_{0.25}$	336	37	328	387	660	118	0.390	7	5	100
		± 4	± 1	± 16	± 19	± 33	± 1				
Substrate-bias series	$Cr_{0.98}N_{0.02}$	347	23	224	225	227	105	0.352	9	10	40
		± 8	± 1	± 11	± 11	± 11	± 1				
	$Cr_{0.86}N_{0.14}$	351	34	302	353	557	110	0.377	8	7	170
		± 7	± 1	± 15	± 17	± 27	± 1				
	$Cr_{0.81}N_{0.19}$	291	26	299	341	458	105	0.351	12	7	70
		± 8	± 1	± 15	± 17	± 22	± 1				

In the substrate-bias series, the film with the lowest amount of h-$Cr_2N_{1-\delta}$ exhibits a low hardness of 23 GPa compared to the values on similar composition in the target-power series (Tables 2 and 3). In the substrate-bias series, a higher amount of h-$Cr_2N_{1-\delta}$ in the film deposited with a lower bias led to a decrease of the hardness to 26 GPa. The hardness values in the two series remains high compared to the mixing rule (bcc-Cr/h-$Cr_2N_{1-\delta}$) and still lying above values reported for $Cr_2N_{0.95}$ coatings which had low microstrain (12 to 21 GPa) [45]. With increasing nitrogen content, the reduced Young's modulus remains between 300 and 350 GPa whereupon it softened by 18% to reach 290 GPa when using a low substrate bias.

The elastic properties extracted from PLU and BLS provided a comparison of the reduced Young's modulus and the values of the shear modulus (Fig. 6c and Table 3). In the Cr rich Cr:N for the target-power series, the reduced Young modulus values from PLU and BLS are comparable with nanoindentation ones (+ 10%) considering the assumptions (isotropic elastic properties, no crystallographic texture contribution, and a homogeneous single-phase film). In the target-power series, Young's and shear varied between E = 299–328 GPa and C_{44} = 110–118 GPa and are comparable with the DFT theoretical prediction of the modulus for bcc-Cr (E = 279 GPa, G = 115 GPa [46]) and CrN (E = 279 GPa, G = 111 GPa [3]). For example, the film containing 37% of h-$Cr_2N_{1-\delta}$ exhibited a Young's and shear modulus of E = 302 GPa and C_{44} = 110 GPa, respectively. On higher addition of h-$Cr_2N_{1-\delta}$ (> 40% in the film for both series), the extracted reduced Young's modulus values from PLU and BLS seems to not correlate with the one measured by nanoindentation. A similar observation can be done for the film with the low h-$Cr_2N_{1-\delta}$ content in the substrate-bias series. In both cases, the values extracted from PLU and BLS might deviate due to assumptions which became inexact due to the secondary phase (h-$Cr_2N_{1-\delta}$) dominating and the apparent density of the film reducing. Moreover, these films may have a higher degree of elastic anisotropy leading to different in plane and out-of-plane Young's modulus and thus differences between the values extracted from nanoindentation or PLU/BLS.

The thermal conductivity measured by thermoreflectance varies between 7 and 12 W/mK. A value of a pure Cr thin metal has been reported to 94 W/mK [47]. The reported thermal conductivity of single phase Cr_2N films measured by the same technique was 12 W/mK [48]. In the present work the thermal conductivity is relatively low compared to the ones from bcc-Cr metal and in the same order as the thermal conductivity of Cr_2N. For information the thermal conductivity measured on the rock salt CrN is at 4 W/mK [17,18].

The electrical resistivity of the sample measured by four-point probe varies between 40 and 170 μΩcm. At low nitrogen content, when the bcc-Cr phase dominates (CrN_3 and CrN_2), the electrical resistivity is higher than the metal reference and can be due to the presence of the secondary phase or the dilution of oxygen/nitrogen into the bcc-Cr phase. At higher nitrogen content, when the content of h-$Cr_2N_{1-\delta}$ increases, the value of the electrical resistivity increases to a maximum of 170 μΩcm before it decreases towards the value of electrical resistivity of Cr_2N.

4. Discussion

All depositions were done using the assistance of a coil at the substrate location in the chamber which led to dense and smooth film of $Cr_{1-x}N_x$. This method allows to increase the adatom mobility at the substrate during growth by tuning the ion/neutral ratio incident at the growing film surface [49]. Compared with conventional dc sputtering, the use of this technique has shown great improvement of the morphology, density and can allow of a control of crystallographic texture [26–28].

In the present study and in both series, variations of the target power or the substrate bias have shown an influence on the nitrogen content in the film (Table 1) along with variation of density, morphology, mechanical, thermal, and electrical properties of the films. The variation of composition of the films in the target-power series are directly connected to the target power applied. A higher target power leads to an increase of the voltage and the current, thus an increase of the sputter yield of Cr with higher bombarding ions. These changes led to films with higher content in chromium and a denser morphology as observed at higher target power (Tables 1 and 2, and Fig. 5). The variation of composition observed in the substrate-bias series is mainly connected the preferential sputtering happening at the substrate. The variation of bias, in combination with the coil, increases the Ar^+ etching at the substrate [30], and increases the stress observed in the film. The use of substrate bias voltage enhanced Ar^+ ion bombardment which causes the re-sputtering of nitrogen adatoms from growing film, in a similar way as the contamination of oxygen is more pronounce for the low substrate bias film [50]. The use of bombardment of high-density Ar^+ ions with varied energy seems to affect drastically the type of growth from columnar growth to nanocrystalline film. Added to the preferential sputtering changing the composition of the film, the competitiveness between the two phases seems to affect the nucleation during growth which seemed to be more pronounce for the film with medium energy of bombardment diminishing the columnar growth.

According to XRD and TEM measurement, the films are composed of a mixture of a bcc-Cr phase plus a phase isotype as h-$Cr_2N_{1-\delta}$ sub-stoichiometric in nitrogen. Both series showed similar existence of phases directly connected to their composition in nitrogen. In a bcc material system, such as Cr or few other 3d transition metals, the structure can accommodate few percent (3–4%) of oxygen, nitrogen, carbon, or boron with a tetragonal distortion and an increase of the cell volume [51–53]. In the present case, the tetragonal distortion could not be observed due to the broadening and the low intensity observed on the 110 reflection from the bcc-Cr. Nevertheless, the possibility that bcc-Cr phase identified in all films could have few percent (< 3–4%) of dissolved nitrogen and/or oxygen was not excluded. For clarity and simplicity, both the pure bcc-Cr phase and the nitrogen-doped bcc-Cr

phase will be denominated as bcc-Cr phase in the following.

All films were deposited on c-plane sapphire and with the mixture of phases, the evaluation of global stress level in the films was problematic. Nevertheless, the constant XRD peak position observed on the bcc-Cr in the target power series reveals a constant level of stress for that phase in that series (Fig. 2b). In the substrate-bias series, the XRD peak position of the bcc-Cr shift from high to low angle when the substrate bias increases from -30 to -100 V revealing an increase of compressive stress (Fig. 3b). For the h-$Cr_2N_{1-\delta}$, the interpretation is delicate having the possibility of variation of nitrogen content in the phase and possibly a variation of stress level for that phase in a similar way as observed for the bcc-Cr. In the target-power series where the bcc-Cr has a constant level of stress, if considering a similar level of stress for both phases, then the shift of the XRD peak position is caused mainly by the variation of the nitrogen vacancies in the h-$Cr_2N_{1-\delta}$ (Fig. 2b). Following the same reasoning for the substrate-bias series, a compressive stress and an increase of nitrogen vacancies in the h-$Cr_2N_{1-\delta}$ would have an opposite effect on the peak position leading to difficult analysis and conclusion (Fig. 3b).

As general observation in both series, the films are composed of a mixture of bcc-Cr and h-$Cr_2N_{1-\delta}$. The stress level seems to be correlated to the substrate bias. At fixed substrate bias of -75 V the stress in the film seem to remain constant in the target-power series, while on increasing the substrate bias, the stress varies to a more compressive stage. The general increase of the stress level with the substrate bias is consistent with the general observation on thin film: a higher substrate bias yield to higher compressive stress in the film [54]. The estimated lower apparent density measured on this film might be due to the competitiveness between bcc-Cr and h-$Cr_2N_{1-\delta}$ phase combined with the higher level of stress created at high substrate bias in Ar^+ ion assisting magnetron sputtering where the Ar ion density at the substrate is larger than common magnetron sputtering.

In the present study, the Cr:N films have their mechanical properties extremely connected to the amount of h-$Cr_2N_{1-\delta}$ phase content in the films, the morphology and the stress level. In the target-power series, the measured hardness values vary between 30 and 36 GPa. With similar morphologies of the film, apparent densities and stress level between the three samples (Tables 2 and 3), the evolution of the hardness increases monotonically with the h-$Cr_2N_{1-\delta}$ content. In the substrate-bias series, extrinsic aspects present, such as differences in apparent densities, possible variations of stress, and possible variations of δ in h-$Cr_2N_{1-\delta}$ phase, make the interpretation and conclusion more difficult. The residual stress seemed to greatly improve the hardness of the films to maximum values of 36 GPa, while a hardness of 26 GPa is measured for similar h-$Cr_2N_{1-\delta}$ containing film with a lower level of residual stress. A lower apparent density combined with columnar growth and higher stress level of the films was critical for the hardness of the film for the lowest nitrogen containing films where the hardness dropped from 30 to 23 GPa.

For comparison, the hardness for the lower nitrogen coating is much higher than the bcc-Cr metal (~10 GPa) [8]. Coatings of a pure bcc-Cr containing 4% of diluted N in the structure has been reported with a 24 GPa hardness [24]. In the other hand, the hardness of pure $Cr_2N_{0.95}$ coatings annealed at different temperatures [150 °C, 700 °C] is within 12 GPa and 21 GPa [45]. According to previous studies, the mechanical properties of Cr:N films can vary greatly as well as for Cr_2N. Cr:N hardness can vary from 15 GPa [6] to 38 GPa [7] depending on sputtering parameters. Mayrhofer et al. [7] showed that composition, grain size and residual stresses are responsible for variation in hardness. Greczynski et al. [24] explained the high hardness of his HiPIMS samples by the reduced grain boundary sliding and a lower dislocations density. The hardness of richer nitrogen coatings is higher than that predicted by the rule of mixtures for 40% bcc-Cr and 60% h-Cr_2N phase given at about 26.5 GPa [56].

According to the diffractograms and the TEM images of our materials, the films are nanocrystalline and small h-$Cr_2N_{1-\delta}$ crystallites should most probably be located between the bcc-Cr grains. This structural arrangement should slow down the motion of dislocations between the grains. The further increase of the hardness might be attributed to the presence of interfaces in these complex nanocomposites which block the dislocation movement [57], rather than the presence of harder h-$Cr_2N_{1-\delta}$ phase in the film. The nanostructure aspect of the composite is also influencing the thermal conductivity and electrical conductivity of the coatings. The low thermal conductivity observed on the Cr-side of the Cr:N system is lower compared to bcc-Cr and Cr_2N and explained by the nanostructuring in the coatings leading to higher phonon scattering. The electrical resistivity values are in the same range but higher than specific resistivity of Cr (15 $\mu\Omega$cm [58]) and Cr_2N (70 $\mu\Omega$cm [48]) which could not be connected to the nitrogen stoichiometry, but mainly by the nanostructuring nature of the sample in which grain boundaries density are increased thus the electrical resistivity.

5. Conclusion

Different films of chromium rich Cr:N coatings (0.03 < N/Cr < 0.33) were deposited at relatively low temperature (200 °C) by reactive DC sputtering in combination with Ar ion assisting magnetron sputtering. The changes in composition controlled by substrate bias or target power led to nanocomposite with varied proportion of bcc-Cr and h-$Cr_2N_{1-\delta}$. The use of Ar ion assisting magnetron techniques diminished the columnar growth usually observed on classical dc-magnetron sputtering leading to dense, non-columnar nanostructure coatings. The mechanical properties, estimated by nanoindentation, complementary Brillouin light scattering in combination with picosecond laser ultrasonics, revealed a higher hardness (between 20 and 38 GPa) and higher reduced Young's modulus (between 300 and 360 GPa) than one can expect from a simple rule of mixture. The films presented relatively low thermal conductivities between 7 and 10 W/mK which are lower than the one of bcc-Cr or h-$Cr_2N_{1-\delta}$. The hardening process, thermal properties and electrical properties of the films were attributed to the multiphase nanostructure happening in this low nitrogen content Cr:N material. The formation of this secondary phase and their distribution in the coatings seems to play a role on the mechanisms affecting the dislocation, phonon, and electron propagation in the film.

CRediT authorship contribution statement

Camille Pallier: Conceptualization, Methodology, Writing original draft preparation, Investigation/Synthesis and material characterization.

Philippe Djemia: Methodology, Writing original draft preparation, Investigation/PLU and BLS.

Daniele Fournier Methodology, Investigation/PLU and BLS.

Laurent Belliard: Funding acquisition/PLU and BLS.

Jun Lu: Methodology, Investigation/TEM.

Fredrik Eriksson: Conceptualization, Methodology/Synthesis.

Per Eklund: Funding acquisition, Supervision, Writing - Review & Editing.

Grzegorz Greczynski: Methodology, Writing - Review & Editing.

Arnaud le Febvrier: Conceptualization, Methodology, Visualization, Writing - Review & Editing.

Declaration of competing interest

The authors declare that they have no known competing financial interests or personal relationships that could have appeared to influence the work reported in this paper.

References

[1] L. Hultman, Vacuum 57 (2000) 1–30.
[2] P.H. Mayrhofer, C. Mitterer, L. Hultman, H. Clemens, Prog. Mater. Sci. 51 (2006) 1032–1114.
[3] H. Kindlund, D.G. Sangiovanni, I. Petrov, J.E. Greene, L. Hultman, Thin Solid Films 688 (2019), 137479.
[4] G. Berg, C. Friedrich, E. Broszeit, C. Berger, Surf. Coat. Technol. 86–87 (1996) 184–191.
[5] P. Djemia, M. Benhamida, K. Bouamama, L. Belliard, D. Faurie, G. Abadias, Surf. Coat. Technol. 215 (2013) 199–208.
[6] P. Hones, N. Martin, M. Regula, F. Lévy, J. Phys. D. Appl. Phys. 36 (2003) 1023.
[7] P.H. Mayrhofer, G. Tischler, C. Mitterer, Surf. Coat. Technol. 142–144 (2001) 78–84.
[8] Z. Zeng, L. Wang, L. Chen, J. Zhang, Surf. Coat. Technol. 201 (2006) 2282–2288.
[9] K. Balasubramanian, S.V. Khare, D. Gall, Acta Mater. 159 (2018) 77–88.
[10] C.S. Shin, Y.W. Kim, D. Gall, J.E. Greene, I. Petrov, Thin Solid Films 402 (2002) 172–182.
[11] G. Abadias, C.-H. Li, L. Belliard, Q.M. Hu, N. Greneche, P. Djemia, Acta Mater. 184 (2020) 254–266.
[12] F. Angay, L. Löfler, F. Tetard, D. Eyidi, P. Djemia, D. Holec, G. Abadias, J. Vac. Sci. Technol. A 38 (2020), 053401.
[13] D. Kim, K. Lee, Y.S. Yoon, Nucl. Eng. Technol. 50 (2018) 724–730.
[14] P. Hones, R. Sanjines, F. Levy, Surf. Coat. Technol. 94–95 (1997) 398–402.
[15] O. Glozman, A. Hoffman, Diam. Relat. Mater. 6 (1997) 796–801.
[16] C.X. Quintela, J.P. Podkaminer, M.N. Luckyanova, T.R. Paudel, E.L. Thies, D. A. Hillsberry, D.A. Tenne, E.Y. Tsymbal, G. Chen, C.-B. Eom, F. Rivadulla, Adv. Mater. 27 (2015) 3032–3037.
[17] M.A. Gharavi, S. Kerdsongpanya, S. Schmidt, F. Eriksson, N.V. Nong, J. Lu, B. Balke, D. Fournier, L. Belliard, A.L. Febvrier, C. Pallier, P. Eklund, J. Phys. D: Appl. Phys. 51 (2018), 355302.
[18] S. Kerdsongpanya, B. Sun, F. Eriksson, J. Jensen, J. Lu, Y.K. Koh, N.V. Nong, B. Balke, B. Alling, P. Eklund, J. Appl. Phys. 120 (2016), 215103.
[19] P. Eklund, S. Kerdsongpanya, B. Alling, J. Mater. Chem. C 4 (2016) 3905–3914.
[20] B. Biswas, S. Chakraborty, O. Chowdhury, D. Rao, A.I.K. Pillai, V. Bhatia, M. Garbrecht, J.P. Feser, B. Saha, Phys. Rev. Mat. 5 (2021), 114605.
[21] G. Greczynski, J. Jensen, L. Hultman, IEEE Trans. Plasma Sci. 38 (2010) 3046–3056.
[22] J.J. Olaya, G. Wei, S.E. Rodil, S. Muhl, B. Bhushan, Vacuum 81 (2007) 610–618.
[23] C. Rebholz, H. Ziegele, A. Leyland, A. Matthews, Surf. Coat. Technol. 115 (1999) 222–229.
[24] G. Greczynski, J. Lu, O. Tengstrand, I. Petrov, J.E. Greene, L. Hultman, Scr. Mater. 122 (2016) 40–44.
[25] A. Baptista, F. Silva, J. Porteiro, J. Míguez, G. Pinto, Coatings 8 (2018) 402.
[26] C. Engström, T. Berlind, J. Birch, L. Hultman, I.P. Ivanov, S.R. Kirkpatrick, S. Rohde, Vacuum 56 (2000) 107–113.
[27] I. Ivanov, P. Kazansky, L. Hultman, I. Petrov, J.E. Sundgren, J. Vac. Sci. Technol. A 12 (1994) 314–320.
[28] I. Petrov, L. Hultman, U. Helmersson, J.E. Sundgren, J.E. Greene, Thin Solid Films 169 (1989) 299–314.
[29] J. Birch, T. Joelsson, F. Eriksson, N. Ghafoor, L. Hultman, Thin Solid Films 514 (2006) 10–19.
[30] F. Eriksson, G.A. Johansson, H.M. Hertz, J. Birch, Opt. Eng. 4506 (2001) 84–92.
[31] A.L. Febvrier, J. Jensen, P. Eklund, J. Vac. Sci. Technol. A 35 (2017), 021407.
[32] G. Greczynski, L. Hultman, ChemPhysChem 18 (2017) 1507–1512.
[33] G. Greczynski, L. Hultman, Appl. Surf. Sci. 542 (2021), 148599.
[34] W.C. Oliver, G.M. Pharr, J. Mater. Res. 7 (1992) 1564–1583.
[35] C. Thomsen, J. Strait, Z. Vardeny, H.J. Maris, J. Tauc, J.J. Hauser, Phys. Rev. Lett. 53 (1984) 989–992.
[36] F. Xu, C. Frétigny, D. Fournier, L. Belliard, S. Vincent, B. Perrin, S. Martin, C. Secouard, J.-Y. Duquesne, J. Appl. Phys. 113 (2013), 244304.
[37] G. Abadias, P. Djemia, L. Belliard, Surf. Coat. Technol. 257 (2014) 129–137.
[38] R. Loudon, Phys. Rev. Lett. 40 (1978) 581–583.
[39] P. Djemia, F. Ganot, P. Moch, V. Branger, P. Goudeau, J. Appl. Phys. 90 (2001) 756–762.
[40] L. Pottier, Appl. Phys. Lett. 64 (1994) 1618–1619.
[41] C. Frétigny, J.P. Roger, V. Reita, D. Fournier, J. Appl. Phys. 102 (2007), 116104.
[42] N. Tureson, M. Marteau, T. Cabioch, N.V. Nong, J. Jensen, J. Lu, G. Greczynski, D. Fournier, N. Singh, A. Soni, L. Belliard, P. Eklund, A.L. Febvrier, Phys. Rev. B 98 (2018), 205307.
[43] Gaithersburg MD, 2000.
[44] W. Ernst, J. Neidhardt, H. Willmann, B. Sartory, P.H. Mayrhofer, C. Mitterer, Thin Solid Films 517 (2008) 568–574.
[45] P. Kringhøj, J. Bøttiger, J. Chevallier, E.J. Bienk, K. Rätzke, Surf. Coat. Technol. 149 (2002) 82–88.
[46] S.F. Pugh, Lond. Edinb. Dublin Philos. Mag. J. Sci. 45 (1954) 823–843.
[47] B. Tlili, C. Nouveau, M.J. Walock, M. Nasri, T. Ghrib, Vacuum 86 (2012) 1048–1056.
[48] M.A. Gharavi, G. Greczynski, F. Eriksson, J. Lu, B. Balke, D. Fournier, A. le Febvrier, C. Pallier, P. Eklund, J. Mater. Sci. 54 (2019) 1434–1442.
[49] I. Petrov, P.B. Barna, L. Hultman, J.E. Greene, J. Vac. Sci. Technol. A 21 (2003) S117–S128.
[50] H. Ljungcrantz, L. Hultman, J.E. Sundgren, S. Johansson, N. Kristensen, J. Å. Schweitz, C.J. Shute, J. Vac. Sci. Technol. A 11 (1993) 543–553.
[51] K. Lee, S. Liguori, P. Psarras, J. Wilcox, J. Phys. Chem. C 121 (2017) 17016–17028.
[52] F.J.M. Boratto, R.E. Reed-Hill, Scr. Metall. 12 (1978) 313–318.
[53] J.-P. Zhou, D. Li, Y.-S. Gu, X.-R. Chang, C.-S. Zhao, F.-S. Li, L.-J. Qiao, Z.-Z. Tian, G.-D. Fang, Q.-S. Song, J. Magn. Magn. Mater. 238 (2002) 1–5.
[54] G. Greczynski, I. Petrov, J.E. Greene, L. Hultman, J. Vac. Sci. Technol. A 37 (2019), 060801.
[55] L. Shan, Y. Wang, J. Li, J. Chen, Surf. Coat. Technol. 242 (2014) 74–82.
[56] L.-S. Zhao, L.-N. Wang, D.-S. Chen, H.-X. Zhao, Y.-H. Liu, T. Qi, Trans. Nonferrous Metals Soc. China 25 (2015) 1325–1333.
[57] J.S. Koehler, Phys. Rev. B 2 (1970) 547–551.
[58] M. Ohashi, K. Ohashi, M. Sawabu, M. Miyagawa, T. Kubota, K. Takanashi, Phys. Lett. A 380 (2016) 3133–3137.